

Andrés A. Peña · Sean McNamara · Pedro G. Lind · Hans J. Herrmann

# Avalanches in anisotropic sheared granular media

Received: date

**Abstract** We study the influence of particle shape anisotropy on the occurrence of avalanches in sheared granular media. We use molecular dynamic simulations to calculate the relative movement of two tectonic plates. Our model considers irregular polygonal particles constituting the material within the shear zone. We find that the magnitude of the avalanches is approximately independent on particle shape and in good agreement with the Gutenberg-Richter law, but the aftershock sequences are strongly influenced by the particle anisotropy yielding variations on the exponent characterizing the empirical Omori's law. Our findings enable one to identify the presence of anisotropic particles at the macro-mechanical level only by observing the avalanche sequences of real faults. In addition, we calculate the probability of occurrence of an avalanche for given values of stiffness or frictional strength and observe also a significant influence of the particle anisotropy.

## 1 Introduction

Natural earthquakes are one of the most catastrophic events in nature [1] with deep social implications, in terms of human casualties and economic loss. Considerable efforts have been made to understand the earthquake dynamics and the underlying mechanisms prior to their occurrence [2; 3; 4; 5], either through experimental studies [6; 7; 8] or through particle based numerical models [9; 10; 11; 12] of the relative motion of tectonic plates [1; 13; 14].

However, in most of the existing numerical models of earthquake fault the gouge is represented by discs [11; 12] or spheres [15]. The dynamics of such material within the

fault is thought to control the stick-slip instability that characterizes earthquake process. An understanding of its properties is, therefore, vital to understand earthquake dynamics [16]. For instance, the existence of the gouge within the fault has been proposed to explain the low dissipation on shear zones, providing new insight into the heat flow paradox [17]. In this case, the reduction of the macroscopic friction and consequently, the heat generation is attributed to the deformational patterns such as rolling of particles [11; 12]. In laboratory experiments by Maron [8], the influence of particle characteristics has also been studied. They found that frictional strength and stability of the granular shear zone is influenced by particle shape, size distribution and their evolution through particle crushing. Therefore, to model fault gouges one must also include different grain characteristics.

In this paper, we use a model of polygonal particles [18; 19] to address the influence of anisotropy in granular media. We study the situation of two tectonic plates with boundaries parallel to the direction along which the tectonic plates move – so-called transform boundaries [1; 14]. One of the most well known examples of such boundaries is the San Andres Fault in California where the Pacific plate and the North American plate are moving in opposite directions. In this particular case, the relative motion of the plates is about 40 mm/year, and thus the strain accumulation rate is around  $3 \cdot 10^{-7}$  per year [20]. Further, different from previous studies [10], our model considers anisotropic particle shapes. The response of the system is characterized by discrete events or avalanches whose size covers many orders of magnitude, similar to the so-called crackling noise of physical systems [21].

We find that the magnitude of the avalanches is independent of the particle shape and in agreement with the Gutenberg-Richter law [22]. On the contrary, the distribution of the waiting times described by the Omori's law [23] strongly depends on shape anisotropy. From this result, we raise the hypothesis of identifying at the macro-mechanical level the presence of anisotropic particles within the gouge, only by studying the temporal avalanche sequences. We further argue that the existence of this anisotropic gouge in fault zones

---

A. A. Peña, S. McNamara, P. G. Lind  
Institute for Computational Physics, Universität Stuttgart, Pfaffenwaldring 27, D-70569 Stuttgart, Germany  
E-mail: andres@icp.uni-stuttgart.de

H. J. Herrmann  
Departamento de Física, Universidade Federal do Ceará, 60451-970 Fortaleza, Ceará, Brazil;  
Computational Physics, IfB, HIF E12, ETH Hönggerberg, CH-8093 Zürich, Switzerland

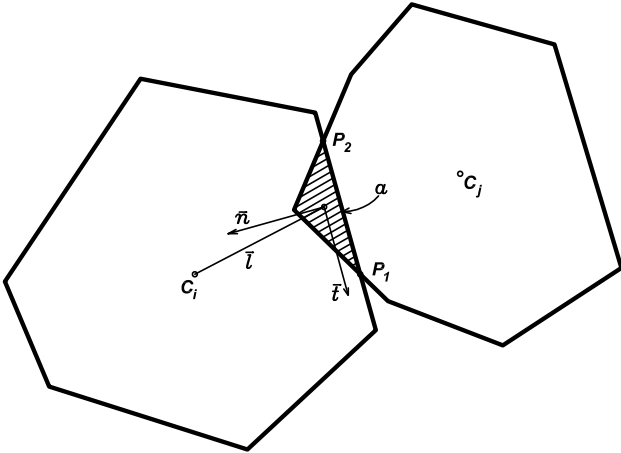


**Fig. 1** Schematic representation of a particle contact. The overlapping area  $a$  is indicated by the shaded zone.

might also explain the variation of the decay of the after-shock sequences observed in nature.

In addition, we also compute the conditional probability for an avalanche to occur, and found that it decreases logarithmically with the stiffness. This exponential decay also depends on particle shape, since anisotropic samples are able to mobilize a higher frictional strength when compared to isotropic samples. For a given value of mobilized strength anisotropic samples also exhibit lower probability of failure. Finally, we propose some microstructural features that could help to explain the occurrence of avalanches.

We start in Sec. 2 by describing in detail our model of irregular particles as well as the details of our numerical experiment. In Sec. 3 we characterize and study the system response. In Secs. 4 and 5 we address the influence of particle anisotropy on the frequency distribution of avalanches and on the width of the time interval where aftershocks occur. The weakening and stability of the system is investigated in Sec. 6, and in Sec. 7 the main conclusions are discussed.

## 2 The model

We consider a two dimensional model of convex polygons to represent the grains of the granular material on a mesoscopic scale. The samples consist of isotropic and anisotropic particles in order to study the influence of particle shape anisotropy on the response of a granular packing under very slow shear.

The deformation of the grains is modeled by letting them overlap, as sketched in Fig. 1. When two polygons overlap, the intersection points between their edges can be defined. The segment that connects these points,  $P_1$  and  $P_2$ , gives the contact line  $\mathbf{S} = P_1P_2$ . The contact force is given by

$\mathbf{f}^c = \mathbf{f}^e + \mathbf{f}^v$ , where  $\mathbf{f}^e$  and  $\mathbf{f}^v$  are the elastic and viscous contribution.

The elastic part of the contact force is decomposed as  $\mathbf{f}^e = f_n^e \hat{\mathbf{n}}^c + f_t^e \hat{\mathbf{t}}^c$ , where  $\hat{\mathbf{n}}^c$  and  $\hat{\mathbf{t}}^c$  are the unitary vectors perpendicular and parallel to the contact line  $\mathbf{S}$  respectively. The normal elastic force is calculated as  $f_n^e = -k_n \delta$ , where  $k_n$  is the normal stiffness, and  $\delta$  the deformation length defined in terms of the overlapping area  $a$  and the length of the contact line,  $\delta = a/|\mathbf{S}|$ . The friction force is given by an elastic force  $f_t^e = -k_t \xi$  proportional to the elastic displacement  $\xi$  at each contact, with  $k_t$  the tangential stiffness. The elastic displacement  $\xi$  is updated as  $\xi = \xi' + \mathbf{v}_t^c \Delta t$ , where  $\xi'$  is the previous length of the spring,  $\Delta t$  is the time step of the molecular dynamic simulation, and  $\mathbf{v}_t^c$  the tangential component of the relative velocity  $\mathbf{v}^c$  at the contact. The length of the tangential spring  $\xi$  may increase during the time that the condition  $f_t^e < \mu f_n^e$  is satisfied. The sliding condition is enforced keeping constant the elastic displacement  $\xi$  when the Coulomb limit condition  $f_t^c = \mu f_n^c$  is reached and  $\mu$  is the interparticle friction coefficient.

The viscous force is calculated as  $\mathbf{f}^v = -m\nu\mathbf{v}^c$ , where  $m$  is the effective mass of the two particles in contact and  $\nu$  the damping coefficient. This force takes into account the dissipation at the contact and it is necessary to maintain the numerical stability of the method.

A suitable closed set of material parameters for this model is the ratio  $k_t/k_n$ , together with the value of the normal stiffness  $k_n$ , the interparticle friction  $\mu$ , and the ratio  $\epsilon_t/\epsilon_n$  between the tangential and normal restitution coefficients.

The random generation of the particles is done by means of a Voronoi tessellation using a reference square lattice, yielding a set of nearly isotropic polygons. By distorting the square lattice in the horizontal and vertical directions, we end up with elongated (i.e. anisotropic) particles. The ratio between the stretching and contracting factors gives us the average aspect ratio  $\lambda$  of the polygons, that is used to characterize the anisotropic shape of the particles.

In Fig. 2 the different initial sample configurations are shown. The isotropic configuration is depicted in Fig. 2a, and the anisotropic ones in Fig. 2b for particles stretched in the same direction of shearing (horizontal direction, sample H) and in Fig. 2c for particles stretched perpendicularly to the shear direction (vertical direction, sample V).

We use samples of two different sizes, with 256 ( $16 \times 16$ ) and 1024 ( $32 \times 32$ ) particles. Periodic boundary conditions are imposed in horizontal direction. A constant horizontal

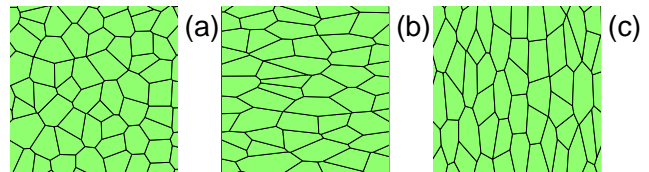


**Fig. 2** (Color online) Samples of (a) isotropic polygons ( $\lambda = 1$ ) and (b) elongated polygons stretched either in the horizontal direction ( $\lambda = 2.3$  H) or (c) in the vertical direction ( $\lambda = 2.3$  V).

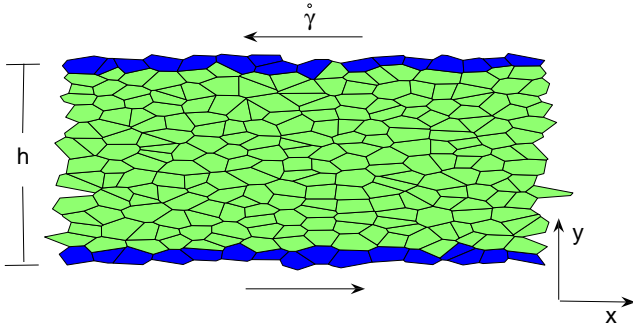


**Fig. 3** (Color online) Sketch of the shear cell. The system is not allowed to dilate, i.e. it has fixed  $h$ . The sample is sheared using a constant shear rate  $\dot{\gamma}$ . Blue (grey) particles induce shear.

velocity is given to the particles in the top and bottom layers so as to impose a constant shear rate  $\dot{\gamma}$ . These particles are not allowed to move in the vertical direction, thus suppressing the volumetric strain of the system. Furthermore, they are not allowed to rotate or move against each other. In Fig. 3 a setup of the shear cell is presented for the anisotropic sample  $\lambda = 2.3$  H. The shear strain  $\gamma$  is defined as

$$\gamma = D_x/h, \quad (1)$$

where  $D_x$  is the horizontal displacement of the boundary particles and  $h$  is the height of the sample, which is kept constant.

In our simple model, polygons represent rocks composing the gauge between two tectonic plates and the top and bottom boundary particles represent the tectonic plates. We start from a perfectly packed configuration in order to represent the initial state of the material that is supposed to be intact prior to the shear process.

As described above, the value of the strain rate is of the order of  $10^{-7}$  per year ( $\approx 10^{-14} \text{ s}^{-1}$ ). For our numerical simulation, this velocity is computationally too expensive. For instance, for  $\Delta t = 1 \text{ s}$  one needs  $10^{12}$  iterations to induce a shear strain of 1%. Using a system of  $16 \times 16$  particles, such  $10^{12}$  iterations would require roughly 1000 years of CPU time on a standard P-IV PC. To overcome this, we choose a suitable shear rate at which the motion of the system is intermittent, i.e. in some regions the system is locked and deforms steadily accumulating elastic strain and in others the stored energy at the contacts is suddenly released. See Fig. 4.

An important issue in this scope is to study the distribution of the released energy, spanned over several orders. We tested shear rates in the range  $10^1 - 10^{-7} \text{ s}^{-1}$  and found that a suitable value for the above purpose is  $\dot{\gamma} = 1.25 \times 10^{-5} \text{ s}^{-1}$ . Further, to perform the MD simulations using the selected shear rate, we adjust the parameters of the model in order to obtain a time step  $\Delta t$  requiring a reasonable CPU time. Thus, we use  $k_n = 400 \text{ N/m}$ ,  $\epsilon_n = 0.9875$ ,  $k_t/k_n = 1/3$ ,  $\nu_t/\nu_n = k_t/k_n$  and  $\epsilon_t/\epsilon_n = 1.0053$ , yielding a time step of  $\Delta t = 0.005 \text{ s}$ . We consider three different interparti-

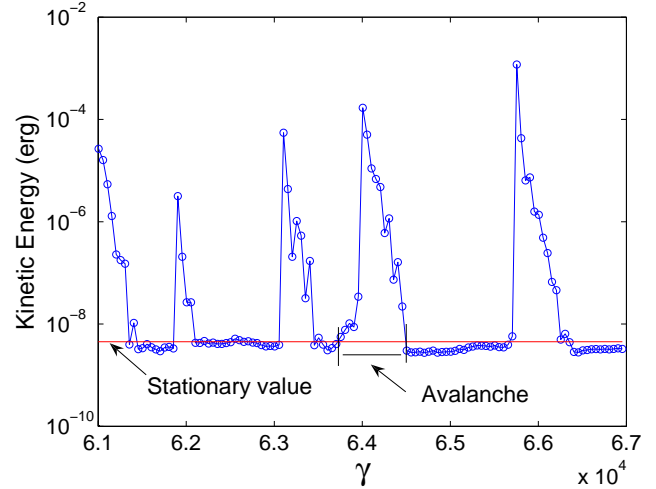


**Fig. 4** (Color online) The average kinetic energy in logarithmic scale versus the shear strain  $\gamma$ . The stationary value  $K_0$  of the kinetic energy is obtained from the velocity profile of the particles at the steady state. The released energy of the avalanches are calculated using Eq. (2).

cle friction coefficients  $\mu = 0.0, 0.5, 5.0$ . For simplicity we use  $\rho = 1 \text{ g/cm}^2$ .

### 3 System response: monitoring avalanches

The motion of the particles in the interior of the sample is not continuous, but has a “stick-slip character”. During slip a sudden rearrangement of the medium arises as a consequence of the large relative displacements of the particles. We monitor this rearrangement of the system through its kinetic energy  $K$ . As shown in Fig. 4, the system can be in two different states. In the “steady state”,  $K$  is approximately equal and less than a low value  $K_0$ , shown by the horizontal line in Fig. 4. This value  $K_0$  is associated with the accumulation of elastic strain under the imposed shear. If the particles were rigid, we would have  $K_0 = 0$ , but since we are using soft elastic ones, we have  $K_0 > 0$ . The low energy state  $K_0$  is punctuated by a series of events where kinetic energy rises several orders of magnitude above  $K_0$ . These are the avalanches. An avalanche begins when  $K$  rises above  $K_0$ , and all subsequent values of  $K$  greater than  $K_0$  are considered to be part of the same avalanche.

The total released energy  $E_r$  of one avalanche is the sum over the total number  $N$  of consecutive values of  $K$  above the stationary state, namely

$$E_r = \sum_{j=1}^N K_j \dot{\gamma} \Delta t, \quad (2)$$

where  $\dot{\gamma} \Delta t$  is a proper non-dimensional parameter for integrating the kinetic energy (see Fig. 4). At the ‘stationary state’ the system is deforming steadily and accumulates energy at the particle contacts. This state can be characterized

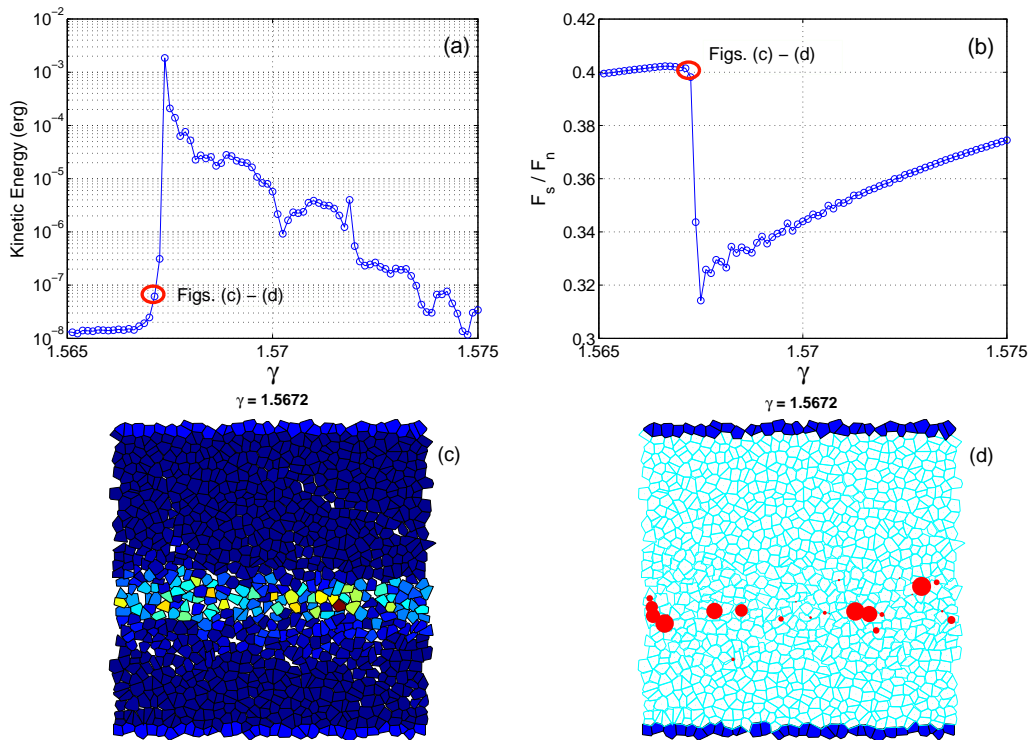


**Fig. 5** (Color online) Accumulation of elastic strain and overcome of the strength  $F_t/F_n$  of the material prior to the occurrence of an avalanche. In (a) the kinetic energy of the system and (b) the ratio  $F_s/F_n$  showing the developed strength are shown, with red circles indicating the strain value at which the snapshot in (c) and (d) are taken. (c) The configuration and accumulated particle rotation just before the avalanche. (d) The elastic strain at the contacts before the avalanche, where the diameter of the red dots is proportional to the value of the deviatoric strain. System size:  $32 \times 32$  particles.

by the value  $K_0$  obtained from the average velocity profile of the particles at this stage.

In the case of infinitely rigid particles, subtracting the ‘stationary value’  $K_0$  from the kinetic energy of the system, one would obtain zero between successive avalanches. Our system is however composed of soft elastic particles, and consequently a non-zero value is observed, as shown in Fig. 4. This non-zero value is a numerical artifact [24] stemming from the calculation of the tangential contact forces, the soft elastic nature of the polygons, and the periodic boundary conditions that can trap some of the energy released during the avalanches. We checked that our present results are not affected by this numerical noise and therefore we will not consider it in anymore detail.

The force needed to sustain the constant motion of the top and bottom layers can be measured in the simulation. In the following,  $F_s$  is the shear (horizontal) force applied to each wall, and  $F_n$  is the normal force. Figure 5 shows the occurrence of one avalanches and the associated strain accumulation for a system with  $32 \times 32$  particles. We can see that the abrupt increment of kinetic energy of the system (Fig. 5a), matches with the fall-off of the strength of the material  $F_s/F_n$ .

Figures 5c and 5d illustrate two different representations of the same sample snapshot, immediately before the avalanche. Figure 5c shows the sample configuration and the rotation that the particles undergo for a shear band located at the center of the sample. The colors of the particles are given by their accumulated rotation: the lighter the color the bigger the accumulated rotation. Figure 5d shows the elastic strain at the contacts, which are represented by red dots with a diameter proportional to its strain value. Here, one can see that there is a strong localization of elastic strain along the shear band. This strain localization weakens the system and drives it to failure, since it promotes the occurrence of the Coulomb limit condition related to the number of sliding contacts (see above). In other words, the weakening of the system is due to both the strain localization and the increase of the ratio of sliding contacts.

During the avalanche the system suffers a complete rearrangement in which the old sliding contacts are removed from the sliding condition and new contacts are generated. This rearrangement marks the beginning of a new stage of elastic strain accumulation that drives the system to the next avalanche.



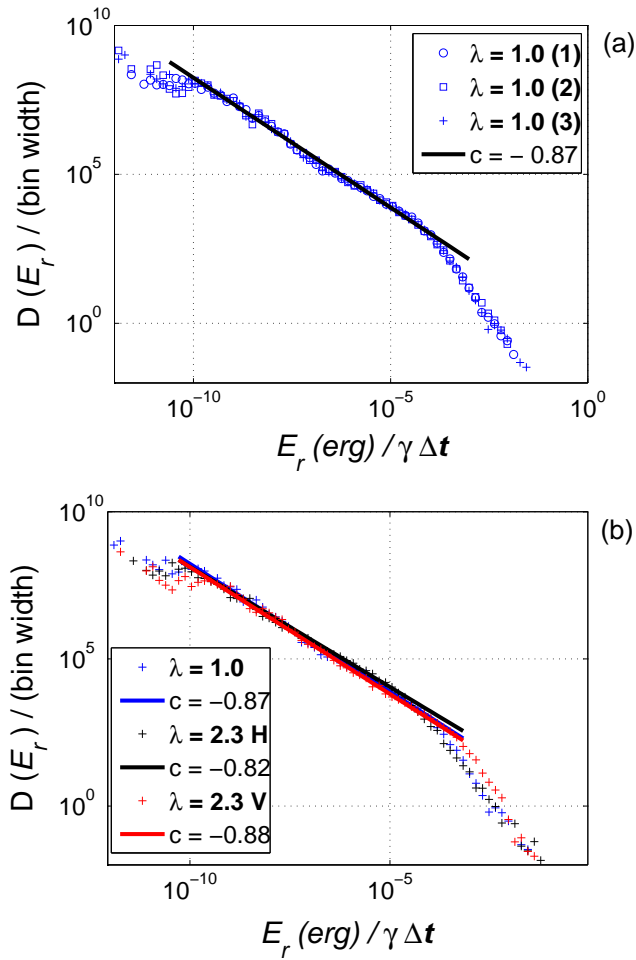


**Fig. 6** (Color online) Log-log plot of the number of avalanches versus their released energy  $E_r$  for (a) different configurations of isotropic particles and (b) for different  $\lambda$  values. Here  $\mu = 0.5$  and the system has  $16 \times 16$  particles. Logarithmic binning is used.

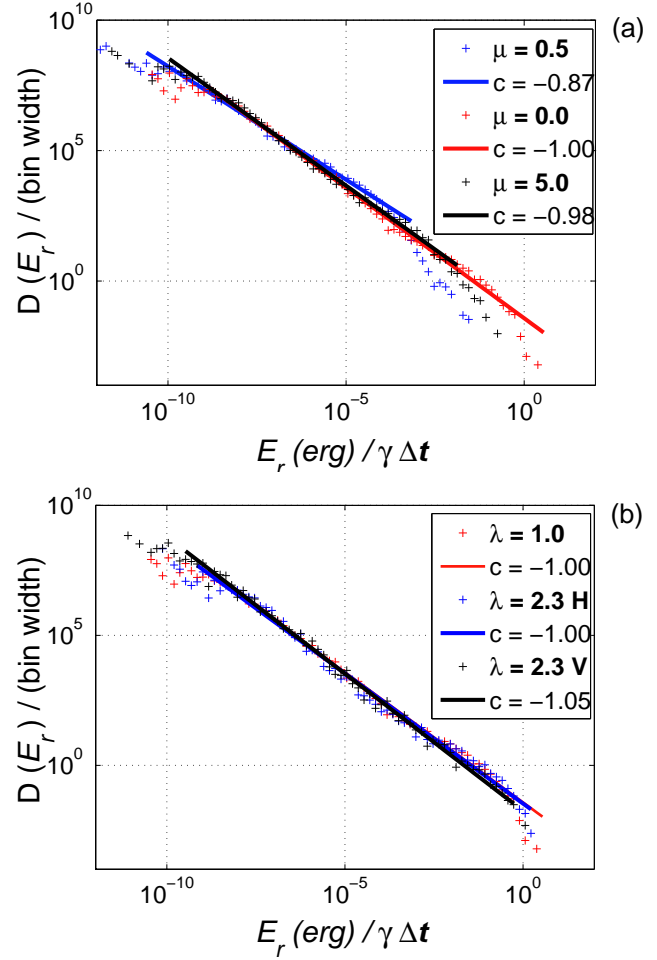


**Fig. 7** (Color online) The distribution  $D(E_r)$  of the released energy  $E_r$  when (a) varying interparticle friction coefficient  $\mu$  with fixed  $\lambda = 1$  and (b) when varying  $\lambda$  with fixed  $\mu = 0$ . The system has  $16 \times 16$  particles and logarithmic binning is used.

#### 4 The Gutenberg-Richter law in anisotropic granular media

The distribution of earthquake magnitude is described by the Gutenberg-Richter law [22]. This law states that the number  $n$  of earthquakes of magnitude  $M$  is proportional to  $n \sim 10^{-bM}$ . Typically, the value of  $b$  is equal to 1 at most places, but may vary between 0.8 and 1.5 [25]. As we will see, the exponent  $b$  will be an invariant property describing the occurrence of avalanches associated with sudden rearrangements of granular media under very slow shear.

To this end, we study the possible influence of the formation and evolution of the shear band on the distribution  $D(E_r)$  of the released energy  $E_r$  during an earthquake. Since the magnitude of an earthquake is defined as the logarithm of the released energy apart proper constants one finds  $n \sim E_r^{-c}$ , with the exponent  $c$  varying typically in the range  $0.8 < c < 1.1$  [25].

In Figure 6a we show the distribution  $D(E_r)$  for three different initial configurations of isotropic samples, corresponding to different seeds for the Voronoi Tessellation. All the distributions collapse and show a power law behavior over almost six orders of magnitude with an exponent of  $c = 0.87$  for the fitted straight line, which is within the observed range of values of the Gutenberg-Richter law.

In Fig. 6b, the distributions for both isotropic and anisotropic particles are shown. Similarly, for all samples, the data sets are well fitted by a power law with an exponent  $c$  ranging from 0.82 to 0.89, indicating a weak influence of the particle shape on the distribution of the released energy. The power law holds over six orders of magnitude.

Similar exponents ( $0.80 < c < 0.95$ ) are obtained for other system sizes in both isotropic and anisotropic cases and for the case when one considers the distribution for individual particles. From such results, one concludes that independent of the anisotropy there is a scale invariance of the system response according to the Gutenberg-Richter law.

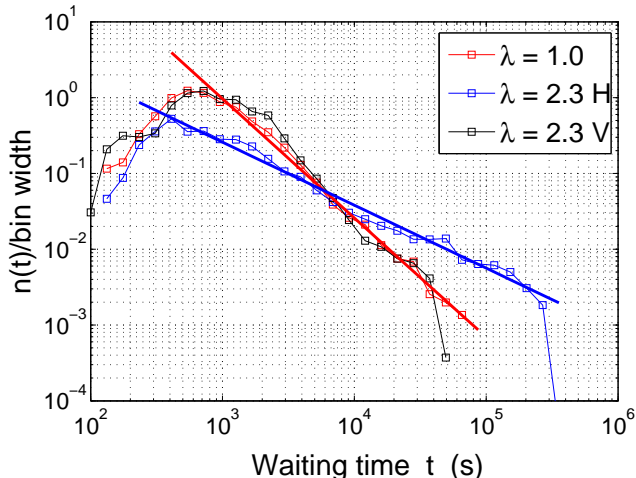


**Fig. 8** (Color online) Distribution  $n(t)$  of waiting times for the sequence of aftershocks in the numerical simulation. Isotropic sample  $\lambda = 1$  and anisotropic samples  $\lambda = 2.3$  are presented. The system has  $16 \times 16$  particles.

We also study the influence of the friction coefficient  $\mu$ . In Fig. 7a the distributions for the isotropic samples with different friction coefficients are plotted. The effect of friction in both cases is to slightly increase the exponent  $c$ , which holds for nearly seven orders of magnitude. The distributions for isotropic and anisotropic samples with  $\mu = 0$  are presented in Fig. 7b where no influence of particle shape is observed.

## 5 Waiting times and Omori's law

Earthquakes usually occur as part of a sequence of events, in which the largest event is called the mainshock and the events prior and after the mainshock are foreshocks and aftershocks respectively [13]. The empirical law that describes the behavior of the temporal sequence of avalanches is called Omori's law, and states that the number  $n(t)$  of aftershocks decreases with the inverse of the time interval  $t$  spanned from the last mainshock as

$$n(t) = \frac{d}{(1+t)^p} \quad (3)$$

where  $d$  is an empirical constant and  $p$  varies in the range  $0.7 < p < 1.5$  [13] with the most typical values around one.

Before performing the calculation of waiting times of aftershocks in the system evolution, we have also to precisely define 'mainshock'. Our definition is based on empirical observations [13]. A new event is considered mainshock only when its released energy is larger than 1/10 of the released energy of the last mainshock. When this happens the sequence of the aftershocks from the previous mainshock is considered to be finished and a new sequence is calculated.

In Fig. 8 the distribution of waiting times for isotropic and anisotropic systems are shown. Over more than three

orders of magnitude all the numerical results can be fitted using the expression in Eq. (3), with exponents  $p = 1.57$  for  $\lambda = 1$ ,  $p = 1.61$  for  $\lambda = 2.3$  V, and  $p = 0.83$  for  $\lambda = 2.3$  H. While for  $\lambda = 2.3$  H one observes an exponent within the typical range found in fault gouges, for  $\lambda = 1$  and  $\lambda = 2.3$  V one finds a clear deviation from the observed values. This indicates not only that anisotropy should be ubiquitous in fault gouges, but also that the most stable configurations are the most common, as explained below.

Using this influence of the initial configuration of anisotropic samples on the stability of the system, we will next explain how to detect at the macro-mechanical level the presence of anisotropic particles within the gouge.

The anisotropic sample  $\lambda = 2.3$  H with particles oriented parallel to the shear direction exhibits a more stable configuration, than the other two cases  $\lambda = 1$  and  $\lambda = 2.3$  V. In this sample, the induced torque on the particles is minimized and the main deformation modes, sliding and rolling of the particles, are highly suppressed by the fixed boundary conditions allowing no dilation in vertical direction. The hindrance of the deformation modes produces a larger temporal stability and also a larger mechanical stability. The larger temporal stability makes the occurrence of the events less frequent in time, i.e. a slower decay of the waiting times. The larger mechanical stability results in a smaller probability of failure for a given value of stiffness as discussed in Sec. 6 below. On the contrary, the configuration of anisotropic samples  $\lambda = 2.3$  V, with particles oriented perpendicular to the shear direction, maximizes the induced torque on the particles and results in a less stable configuration. This configuration yields smaller temporal and mechanical stability. The smaller temporal stability is observed in the decay of the waiting times, that is slightly faster than the one of the isotropic sample. The smaller mechanical stability of sample  $\lambda = 2.3$  V is manifested in the larger probability of failure for a given value of stiffness compared to the other samples.

Therefore, by looking at the decay rate of the aftershock sequences one might be able to explain the variation of the exponent  $p$  in realistic earthquake sequences, by the existence of anisotropic gouge in the fault zone. It is important to say that for a more realistic representation of the earthquake process the crushing of particles should also be taken into account. Nevertheless, the absence of particle crushing is a suitable approximation for the case of young fault gouges.

## 6 Weakening and mechanical stability of the system

In this section we study the relationship between the occurrence of avalanches and the weakening of the system. The weakening process results from the release of energy due to previous accumulation of strain at the contact level and contacts reaching the sliding condition.

In Fig. 9 we show the relative number of sliding contacts  $n_s$ , the stored energy at the contacts  $E_s$  and the total kinetic energy  $E_r$ . The stored elastic energy  $E_s$  at the contacts is calculated as  $E_s = 1/2 (k_n \delta^2 + k_t \xi^2)$ , where  $\delta$  and  $\xi$  are

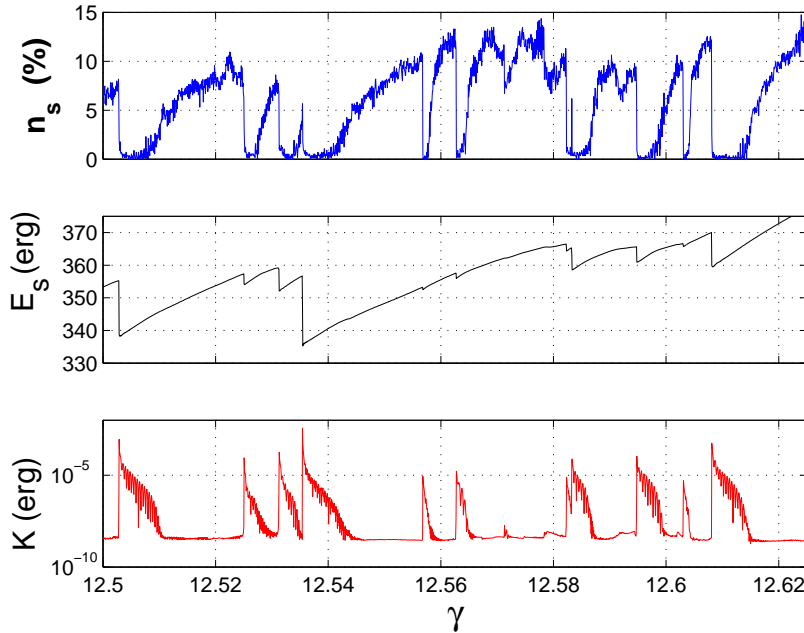


**Fig. 9** (Color online) Evolution of the relative number  $n_s$  of sliding contacts, the energy  $E_s$  stored at the contacts and the total kinetic energy  $E_r$  as a function of the shear strain  $\gamma$ , for an isotropic sample ( $\lambda = 1$ ).

the spring elongations in the normal and tangential directions respectively. Figure 9 shows that between avalanches the relative number of sliding contacts increases with the shear strain. It makes the system weaker and indicates that the system is constantly accumulating elastic energy  $E_s$  at the contacts. The weakening of the system persists until failure, where the kinetic energy increases by several orders of magnitude. At this stage, the structure of the system is rearranged, the stored energy at the contacts is released and the contacts do not fulfill the sliding condition. All the events in the kinetic energy are associated with both drops in the ratio  $n_s$  and drops in the stored energy.

At the macromechanical level the weakening of the system is observed by looking at the evolution of the shear stress with the shear strain. After each stress drop the system experiences a rearrangement. This new configuration produces a temporal stability, in which the strength builds up. At this stage the system sticks and the accumulation of strain takes place. In this softening regime the system approaches failure and when the strength of the material is overcome, the system slips.

The mechanical stability of the system is studied through the stiffness value  $\Delta\tau/\Delta\gamma$  that the system presents at failure. To this end, we calculate the conditional probability  $P(A_E|\Delta\tau/\Delta\gamma)$  for the occurrence of an avalanche event  $A_E$  given a stiffness value  $\Delta\tau/\Delta\gamma$ . Since data only provides the complementary conditional probability  $P(\Delta\tau/\Delta\gamma|A_E)$  we use the Bayes theorem [26], to obtain

$$P(A_E|\Delta\tau/\Delta\gamma) = \frac{P(\Delta\tau/\Delta\gamma|A_E)P(A_E)}{P(\Delta\tau/\Delta\gamma)}. \quad (4)$$

Having a certain time increment  $dt$  in the data, the conditional probability  $P(\Delta\tau/\Delta\gamma|A_E)$  gives the probability of observing a stiffness value  $\Delta\tau/\Delta\gamma$  at  $t - dt$  when at time  $t$  an avalanche (symbolized by  $A_E$ ) occurs. The conditional probability takes into account all the avalanches  $A_E$  within a total time interval of  $5 \cdot 10^6$  s. To this end, we discretize the total time interval in time increments of  $dt = \Delta\gamma/\dot{\gamma}$ . Since the shear rate  $\dot{\gamma} = 1.25 \cdot 10^{-5} \text{ s}^{-1}$  and  $\Delta\gamma = 0.0016$ , the time increment is  $dt = 128$  s is also constant in our simulation. We select the same  $dt$  for both isotropic and anisotropic systems. The probability  $P(A_E)$  is fraction between the total number of avalanches and the total number of time increments, and similarly  $P(\Delta\tau/\Delta\gamma)$  is the probability distribution of  $\Delta\tau/\Delta\gamma$ . In Fig. 10, the conditional probabilities  $P(A_E|\Delta\tau/\Delta\gamma)$  and  $P(\Delta\tau/\Delta\gamma|A_E)$  for both the isotropic system  $\lambda = 1$  and the anisotropic system  $\lambda = 2.3$  are shown. For all the samples, the conditional probability  $P(A_E|\Delta\tau/\Delta\gamma)$  decreases logarithmically with the stiffness: the stiffer the system the smaller is the probability of failure, as shown in Fig 10a, yielding

$$P(A_E|\Delta\tau/\Delta\gamma) \sim q \log(\Delta\tau/\Delta\gamma). \quad (5)$$

Further, from Figs. 10a and 10b, anisotropic samples compared to the isotropic ones explore a different range of stiffness at failure due to the larger rotational frustration that the elongated particles undergo. This is specially true for particles oriented along the shear direction ( $\lambda = 2.3$  H), due to its more stable structure. The exponents of the tail of the distributions are  $q = -42.1$  for  $\lambda = 1$ ,  $q = -28.6$  for  $\lambda = 2.3$  V and  $q = -30.78$  for  $\lambda = 2.3$  H (see Fig. 10a).

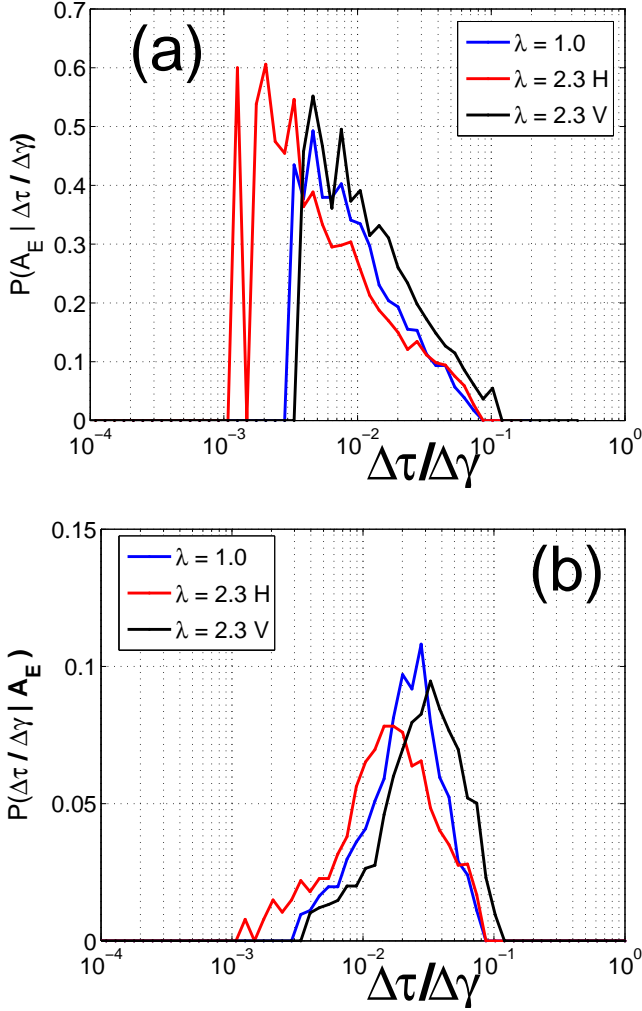


**Fig. 10** (Color online) Conditional probability distributions (a)  $P(A_E | \Delta\tau/\Delta\gamma)$  of the occurrence of an avalanche  $A_E$  given a stiffness  $\Delta\tau/\Delta\gamma$  and (b)  $P(\Delta\tau/\Delta\gamma | A_E)$  of having a stiffness  $\Delta\tau/\Delta\gamma$  at the occurrence of an avalanche. System size  $16 \times 16$ . Isotropic  $\lambda = 1$  and anisotropic samples  $\lambda = 2.3$  are presented. Labels  $H$  and  $V$  correspond to horizontal and vertical samples.

The same analysis can be performed for the occurrence of an avalanche  $A_E$  given a force ratio  $F_s/F_n$  value. In Figure 11, the conditional probabilities  $P(A_E | F_s/F_n)$  and  $P(F_s/F_n | A_E)$  for the same cases as in Fig. 10. As shown in Fig. 11a, the conditional probability  $P(A_E | F_s/F_n)$  increases approximately linearly with  $F_s/F_n$ : The higher the mobilized strength  $F_s/F_n$  the higher the probability of failure. In general, the anisotropic samples are able to mobilize higher frictional strength than the isotropic sample and, for the same force ratio, present a lower probability  $P(A_E | F_s/F_n)$ . This is certainly due to the influence of particle shape anisotropy on the global strength of the material [19].

The probability distribution  $P(F_s/F_n | A_E)$  shown in Fig. 11b of having a force ratio  $F_s/F_n$  at the occurrence of an avalanche  $A_E$  follows typically a normal distribution,

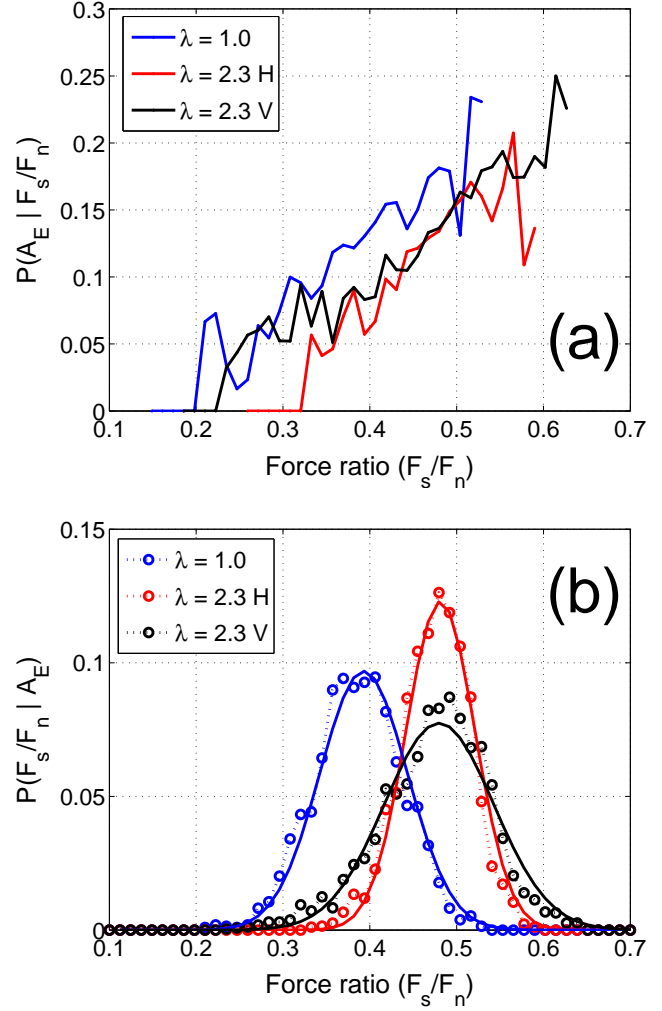


**Fig. 11** (Color online) Conditional probability distributions (a)  $P(A_E | F_s/F_n)$  of the occurrence of an avalanche  $A_E$  given a frictional strength  $F_s/F_n$  and (b)  $P(F_s/F_n | A_E)$  of having a frictional strength  $F_s/F_n$  at the occurrence of an avalanche. System size  $16 \times 16$ . Isotropic  $\lambda = 1$  and anisotropic samples  $\lambda = 2.3$  are presented. Labels  $H$  and  $V$  correspond to horizontal and vertical samples. The  $P(F_s/F_n | A_E)$  follows a normal distribution, except for sample  $\lambda = 2.3 V$ . Solid lines represent the normal distribution of the data.

with a mean value larger in the anisotropic samples. Considering only the anisotropic cases, while one observes the same mean, the standard deviation is larger for the less stable configuration  $V$ , as expected.

Finally, in Figure 12 the sliding contact ratio  $n_s$  and the stiffness at failure of the system are presented. The stiffness is also compared to the released energy of the avalanches. Although no clear correlation between the parameters can be observed, the maximum value of stiffness that the system can present is bounded by  $n_s$ , as illustrated in Fig. 12a. Larger  $n_s$  implies smaller stiffness. In Fig. 12b one sees a weak correlation between the stiffness and the released energy, with a slight tendency of  $E_r$  increasing with the stiff-



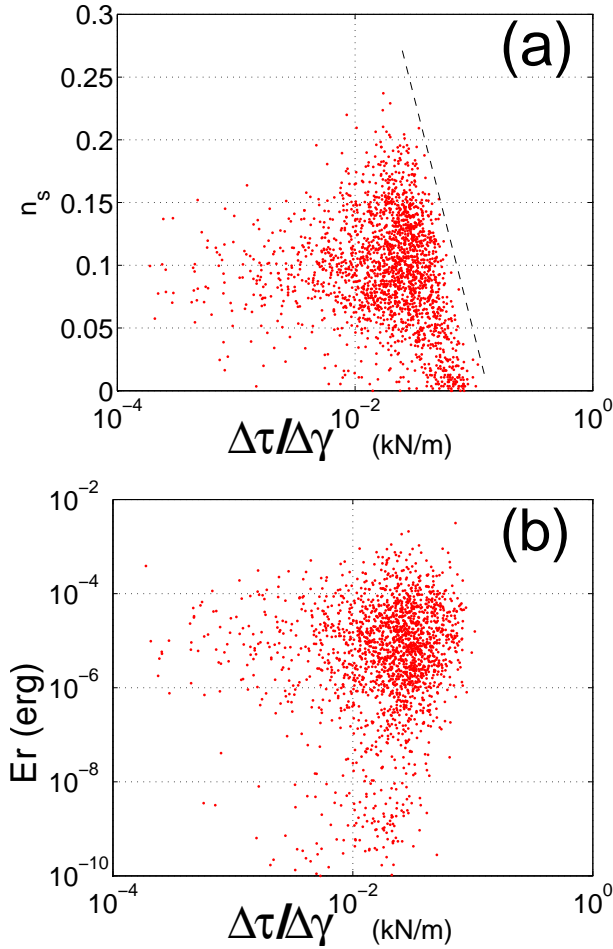


**Fig. 12** (Color online) Relationship between (a) sliding contact ratio  $n_s$  vs. stiffness at failure, (b) released energy  $E_r$  of the avalanche vs stiffness at failure. Data correspond to an isotropic sample with size  $16 \times 16$  particles.

ness. From these observations, it is clear that the accumulation of strain at the contacts is not the only important agent in the weakening process. Therefore, additional ingredients have to be taken into account for a more exhaustive analysis.

## 7 Concluding remarks

In this paper we highlighted the importance of particle shape on the occurrence of avalanches in granular systems. To this end, we used shear cells with periodic boundary conditions to mimic the behavior of tectonic faults with fixed boundaries.

We found that the dynamics of the granular system is characterized by discrete avalanches spanning several order of magnitude similar to crackling noise [2; 21]. We calculated the probability distribution of the energy released in avalanches, and found it to be in very good agreement with

the Gutenberg-Richter law for samples with different particle anisotropy and different system sizes. Consequently the exponent of the released energy distribution can be seen as an invariant property of such systems.

We also studied the temporal distribution of event sequences after a mainshock. We found that the number of aftershocks decreases with a power of the inverse of time. We could fit the sequences of waiting times of the aftershocks with the empirical expression and obtained exponents in the range  $0.7 < p < 1.6$ , similarly to what is observed in real observations according to Omoris law. The anisotropic sample H exhibits a larger temporal stability making the temporal occurrence of the avalanches sparser, due to its larger frustration of rotation in the corresponding initial configuration.

The larger temporal stability observed at the macro-mechanical level can be therefore taken as an indication of the existence of anisotropic material within the shear zone. This could potentially explain the variation of the exponent  $p$  observed in realistic earthquake sequences.

The dynamics of the system was also related to the stick-slip process [27; 28]. When one avalanche begins the system slips, while between two successive avalanches, the system sticks, accumulates elastic energy, and becomes weaker because of the increase of the sliding contacts  $n_s$ . We characterized the weakening of the system by the stiffness  $\Delta\tau/\Delta\gamma$  and derived the conditional probability  $P(A_E|\Delta\tau/\Delta\gamma)$  for an avalanche to occur given a stiffness value  $\Delta\tau/\Delta\gamma$ . We found that  $P(A_E|\Delta\tau/\Delta\gamma)$  decreases logarithmically with the stiffness and with a decay rate larger for isotropic samples than for anisotropic ones. Concerning frictional strength we found that the probability of an avalanche to occur increases with the force ratio  $F_s/F_n$ .

The results concerning the conditional probabilities uncovered that anisotropic samples can explore a wider range of stiffnesses and force ratios than the isotropic sample. This is due to the larger kinematic constraint that anisotropic particles undergo during shear. Further, in general, since the initial configuration corresponding to sample H is the most stable configuration with respect to shearing, it is the one with lower probability of failure.

In previous works concerning the avalanches in granular piles [29; 30], some avalanche precursors associated to the onset of fluidized regions of sliding contacts were found. These fluidized regions were located in the weak network of contacts. This weak network comprises contacts transmitting forces smaller than the average force and therefore has a minimal contribution to the stress state [31; 32]. It is known that [29; 32; 33], while the strong contact network is responsible for the strength and stability of the packing, the weak contact network plays an important role in the destabilization process. In this scope, since precursors are expected to be related to sharp changes in the micro-structure of the granular packing [34], it would be important to study also the network of contact forces as a function of the anisotropy, in particular as a function of the major axis orientation.

Finally, although the results from our numerical model show good agreement with the processes observed in na-

ture, we are aware of the challenges to have a more realistic simulation of fault zones [36]. In future work one should also extend this approach to the three-dimensional case, consider the development of transparent (or absorbing) boundary condition, since the acoustic emission after an avalanche are trapped due to the periodic boundary conditions, and also implement the grain fragmentation, since natural earthquakes result from the combined effect of frictional instabilities and rock fragmentation.

**Acknowledgements** The authors thank L. Arcangelis for useful discussions and also the support by German-Israeli Foundation and by *Deutsche Forschungsgemeinschaft*, under the project HE2732781. PGL thanks support by *Deutsche Forschungsgemeinschaft*, under the project LI 1599/1-1. HJH thanks the Max Planck prize.

## References

1. Bolt BA (2005), Earthquakes. W.H. Freeman and Company, New York.
2. Sykes LR, Shaw BE and Scholz CH (1999) Rethinking earthquake prediction. *Pure Appl. Geophys.*, 155: 207-232.
3. Donz  F, Mora P and Magnier S.-A. (1994) Numerical simulation of faults and shear zones. *Geophys. J. Int.*, 116: 46-52.
4. Mora P and Place D (2002) Stress correlation function evolution in lattice solid elasto-dynamic models of shear and fracture zones and earthquake prediction. *Pure Appl. Geophys.*, 159: 2413-2427.
5. Ramos O, Altshuler E, Mal y KJ (2007) Predicting power law distributed avalanches: implications for earthquake forecast. Private report.
6. Summers R and Byerlee JD (1977) A note on the effect of fault gouge composition on the stability of frictional sliding. *Int. J. Rock Mech. Min. Sci.*, 14: 155-160.
7. Marone C (1998) Laboratory-derived friction laws and their application to seismic faulting. *Annual Review of Earth and Planetary Sciences*, 26: 643-696.
8. Mair K, Frye KM and Marone C (2002) Influence of grain characteristics on the friction of granular shear zones. *J. Geophys. Res.*, 107: 2219.
9. Mora P and Place D (1994) Simulation of the frictional stick-slip instability. *Pageoph.*, 143: 61.
10. Tillemans HJ and Herrmann HJ (1995) Simulating deformations of granular solids under shear. *Physica A*, 217: 261-288.
11. Mora P and Place D (1999) The weakness of earthquake faults. *Geophys. Res. Lett.*, 26: 123-126.
12. Alonso-Marroqu n F, Vardoulakis I, Herrmann HJ, Weatherley D, and Mora P (2006) Effect of rolling on dissipation in fault gouges. *Phys. Rev. E*, 74: 031306.
13. Scholz CH (2002) The mechanics of earthquakes and faulting. Cambridge Univ. Press, Cambridge.
14. Turcotte DL and Schubert G (2002) Geodynamics. Cambridge University Press, Cambridge.
15. Abe S, Latham S and Mora P (2006) Dynamic rupture in a 3-d particle-based simulation of a rough planar fault. *Pure Appl. Geophys.*, 163: 1881-1892.
16. Wilson B, Dewers T, Reches Z and Brune J (2005) Particle size and energetics of gouge from earthquake rupture zone. *Nature*, 434: 749-752.
17. Mora P and Place D (1998) Numerical simulation of earthquake faults with gouge: toward a comprehensive explanation for the heat flow paradox. *J. Geophys. Res.*, 103: 21067-21089.
18. Pe a AA, Lizcano A, Alonso-Marroqu n F and Herrmann HJ (2007) Biaxial test simulations using a packing of polygonal particles. *Int. J. Numer. Anal. Meth. Geomech.*, accepted.
19. Pe a AA, Garc a-Rojo R and Herrmann HJ (2007) Influence of particle shape on sheared dense granular media. *Granular Matter*, 9: 279-291.
20. Kanamori H and Brodsky EE (2001) The physics of earthquakes. *Physics today*, 54: 34-40.
21. Sethna JP, Dahmen KA and Myers CR (2001) Crackling noise. *Nature*, 410: 242-250.
22. Gutenberg B and Richter CF (1954) Seismicity of the Earth and Associated Phenomena. Princeton Uni. Press, Princeton.
23. Omori F (1895) On the aftershocks of earthquakes. *J. Coll. Sci. Imper. Univ. Tokyo*, 7: 111.
24. Pe a AA, Lind PG, McNamara S and Herrmann HJ (2007) Numerical improvement of the discrete element method applied to shear of granular media. Submitted to *Acta Mechanica*, cond-mat arXiv:0709.3716v1.
25. Chakrabarti KB and Benguigui LG (1997) Statistical physics of fracture and breakdown in disordered systems. Clarendon, Oxford.
26. Papoulis A (2002) Probability, random variables, and stochastic processes. McGraw-Hill, Boston.
27. Nasuno S, Kudrolli A, Bank A, and Gollub JP (1998) Time-resolved studies of stick-slip friction in sheared granular layers. *Phys. Rev. E*, 58: 2161-2171.
28. Feder HJS and Feder J (1991) Self-organized criticality in a stick-slip process. *Phys. Rev. Lett.*, 66: 2669-2672.
29. Staron L and Radjai F (2005) Friction versus texture at the approach of a granular avalanche. *Phys. Rev. E*, 72: 041308.
30. Staron L, Vilotte JP and Radjai F (2002) Preavalanche instabilities in a granular pile. *Phys. Rev. Lett.*, 89: 204302.
31. Radjai F, Jean M, Moreau JJ and Roux S (1996) Force distribution in dense two-dimensional granular systems. *Phys. Rev. Lett.*, 77: 274.
32. Radjai F, Wolf DE, Jean M and Moreau JJ (1998) Bimodal character of stress transmission in granular packings. *Phys. Rev. Lett.*, 80: 61-64.
33. Majmudar TS and Behringer RP (2005) Contact force measurements and stress-induced anisotropy in granular materials. *Nature*, 435: 1079-1082.
34. Staron L, Radjai F and Vilotte JP (2006) Granular micro-structure and avalanche precursors. *J. Stat. Mech.*, P07014.
35. Peters JF, Muthuswamy M, Wibowo J and Tordesillas A (2005) Characterization of force chains in granular material. *Phys. Rev. E*, 72: 041307.
36. Alonso-Marroqu n F, Pe a AA, Herrmann HJ and Mora P (2007) Simulation of shear bands using polygonal particles. *Discrete Element Methods (DEM) Conference*.